AGU PUBLICATIONS

JGR

Journal of Geophysical Research: Atmospheres

RESEARCH ARTICLE
10.1002/2016JD025235

Special Section:
Fast Physics in Climate Models: Parameterization, Evaluation and Observation

Key Points:
- Coupled model of convective gravity wave forcing and three-dimensional propagation was developed
- Different scales of convective GW show remarkable difference in spectra and momentum flux distributions
- Found very good agreement with satellite observations specifically in the tropics

Correspondence to:
S. Kalisch,
s.kalisch@fz-juelich.de

Citation:
Kalisch, S., H.-Y. Chun, M. Ern, P. Preusse, Q. T. Trinh, S. D. Eckermann, and M. Riese (2016), Comparison of simulated and observed convective gravity waves, *J. Geophys. Res. Atmos.*, *121*, 13,474–13,492, doi:10.1002/2016JD025235.

Received 15 APR 2016
Accepted 10 NOV 2016
Accepted article online 16 NOV 2016
Published online 28 NOV 2016

Comparison of simulated and observed convective gravity waves

S. Kalisch[1,2], H.-Y. Chun[2], M. Ern[1], P. Preusse[1], Q. T. Trinh[1], S. D. Eckermann[3], and M. Riese[1,4]

[1]Institute of Energy and Climate Research, IEK-7: Stratosphere, Jülich, Germany, [2]Department of Atmospheric Science, Yonsei University, Seoul, South Korea, [3]Naval Research Laboratory, Washington, District of Columbia, USA, [4]Institute of Atmospheric and Environmental Research, University of Wuppertal, Wuppertal, Germany

Abstract Gravity waves (GWs) from convection have horizontal wavelengths typically shorter than 100 km. Resolving these waves in state-of-the-art atmospheric models still remains challenging. Also, their time-dependent excitation process cannot be represented by a common GW drag parametrization with static launch distribution. Thus, the aim of this paper is to investigate the excitation and three-dimensional propagation of GWs forced by deep convection in the troposphere and estimate their influence on the middle atmosphere. For that purpose, the GW ray tracer Gravity-wave Regional Or Global Ray Tracer (GROGRAT) has been coupled to the Yonsei convective GW source model. The remaining free model parameters have been constrained by measurements. This work led to a coupled convective GW model representing convective GWs forced from small cells of deep convection up to large-scale convective clusters. In order to compare our simulation results with observed global distributions of momentum flux, limitations of satellite instruments were taken into account: The observational filter of a limb-viewing satellite instrument restricts measurements of GWs to waves with horizontal wavelengths longer than 100 km. Convective GWs, however, often have shorter wavelengths. This effect is taken into account when comparing simulated and observable GW spectra. We find good overall agreement between simulated and observed GW global distributions, if superimposed with a nonorographic background spectrum for higher-latitude coverage. Our findings indicate that parts of the convective GW spectrum can indeed be observed by limb-sounding satellites.

1. Introduction

Gravity waves (GWs) are well known to affect large-scale circulations like the Brewer-Dobson circulation and the quasi-biennial oscillation [*Lindzen and Holton*, 1968; *Lindzen*, 1981] and contribute significantly to the mesospheric momentum budget. Propagation, dissipation, and breaking of GWs have been in focus of research for many years and therefore achieved a high level of comprehension [*McLandress*, 1998; *Fritts and Alexander*, 2003]. However, their excitation at source level still remains relatively uncertain. This is particularly true for dynamic sources like deep convection. The general importance of convectively forced GWs led to an ongoing development of parametrizations for GW drag from deep convection (GWDC) [*Chun and Baik*, 1998; *Beres et al.*, 2004; *Song and Chun*, 2005]. Further studies [*Chun et al.*, 2004; *Beres et al.*, 2005; *Song et al.*, 2007] have shown the importance of GWDC parametrization to achieve more realistic simulations of the middle atmosphere [*Richter et al.*, 2010; *Kim et al.*, 2013]. One restriction of these parametrizations is the common limitation of GW dynamics to one vertical column albeit some studies already showed their shortcomings compared to ray-based GW drag parametrizations [*Song and Chun*, 2008; *Senf and Achatz*, 2011]. This particular simplification is useful for the development of GW parametrizations [*Charron et al.*, 2002] and reduces computational costs. In contrast, high-resolution general circulation models (GCMs) can resolve some parts of the GW spectrum with wavelengths shorter than 200 km [*Sato et al.*, 2013; *Liu et al.*, 2014]. More recently, *Kalisch et al.* [2014] found that differences caused by the vertical-only propagation assumption are nonnegligible. For that reason we developed a coupled model of convective GW excitation and three-dimensional propagation. The aim of this work is to achieve a more realistic representation of convective GW forcing and their propagation up to the mesosphere.

In this study we focus specifically on the influence of convectively forced GWs and their interaction with middle-atmosphere tropical winds. For this purpose, we applied the Yonsei convective GW source model [*Song and Chun*, 2005; *Song et al.*, 2007; *Choi and Chun*, 2011] as the source model for ray tracing calculations using the GROGRAT ray tracer [*Marks and Eckermann*, 1995]. We also present a comparison with GW momentum flux data from the SABER (Sounding of the Atmosphere using Broadband Emission Radiometry) [*Mlynczak*, 1997; *Russell et al.*, 1999; *Yee et al.*, 2003; *Remsberg et al.*, 2008]) instrument on board of the TIMED (Thermosphere, Ionosphere, Mesosphere Energetics and Dynamics) satellite. The SABER instrument is able to detect GWs with wavelengths as short as 100 km [*Preusse et al.*, 2002; *Alexander et al.*, 2010; *Ern et al.*, 2011]. Further, the visibility function of the instrument is responsible for an underestimation of GW momentum flux in the short horizontal wavelength part of the spectrum and therefore introduces a low bias in the resulting momentum flux where GWs with short horizontal wavelengths are prominent. We repeat the analysis of the ray-traced GWs with a simple "observational filter" in order to estimate the missing part due to instrument restrictions. The aim is to simulate the tropical GW spectrum as seen from SABER to evaluate our findings with these real satellite observations. This strategy provides first insights about the part of the GW spectrum which is, in general, visible to the instrument and about the parts of the spectrum which have to be evaluated by different measurement techniques (e.g., balloon and radio sondes).

Since the Yonsei convective GW source model was also designed to run within a general circulation model (GCM), a few parameters of the model are free for tuning purposes. Two parameters (δ_h and δ_t) represent the spatial and temporal scales of the convective GW source scheme. These parameters can be utilized to tune the model toward different types of forcing ranging from small convective cells to large long-lasting clusters of convection. Additionally, the wave filtering and resonance factor [*Song and Chun*, 2005] accounts for the efficiency of GW forcing and can be used to quantitatively fit GW source model results to observational data. Since the source model estimates GW amplitudes only at launch location (cloud top height), the GROGRAT GW ray tracer [*Marks and Eckermann*, 1995] was used for the subsequent trajectory and amplitude calculations. The combination of the source model and the ray tracer offers the opportunity to distinguish between the influence of (tropical) deep convection and wind filtering effects during the excitation and further propagation of the simulated GWs. Consequently, in this study we focus on the influence of convectively forced GWs and their interaction with tropical winds. Finally, we compare our simulation results with SABER measurements over a wide latitude range by using an additional GW background parametrization for the extratropics and high latitudes.

This paper is organized as follows: Section 2 briefly introduces the model of convective GW sources used for our study. Section 3 describes the coupled model of convective GW source and the GROGRAT ray tracer. Limitations of satellite measurements in limb-sounding geometry are explained in section 4. GW momentum flux, drag, and temperature amplitudes from our simulation are analyzed in section 5 without observational filter and in section 6 with observational filter. A direct comparison between satellite data and our simulation results is presented in section 7. Finally, major findings and conclusions are summarized in section 8.

2. Model Description

Chun and Baik [1998] formulated a parametrization of convectively forced GWs for a vertically uniform background wind in a stable (neglecting turbulent shear flows) atmosphere. This parametrization significantly contributed to the zonal background wind and temperature of the Yonsei atmospheric general circulation model [*Chun et al.*, 2001] and the National Center for Atmospheric Research, Boulder, Colorado (USA) Climate Model 3 [*Chun et al.*, 2004]. These first attempts to include convection as a source of GWs considered only GWs stationary with respect to a moving cloud and were therefore not able to account for GWs with higher phase speeds (e.g., 30 m/s and faster) above cumulus clouds that have been observed and simulated [*Fovell et al.*, 1992; *Pfister et al.*, 1993; *Preusse et al.*, 2001; *Beres et al.*, 2002; *Ern and Preusse*, 2012; *Ern et al.*, 2013]. The analytic formulation of diabatic GW forcing [*Song and Chun*, 2005] solves the limitations of *Chun and Baik* [1998] and also accounts for deep convective forcing. Further applications of this model showed its performance in comparison with satellite observations [*Choi et al.*, 2009, 2012]. However, depending on the observational technique and the model used, different scales have to be considered. Horizontal wavelengths of GWs may range from a few kilometers [*Fovell et al.*, 1992; *Piani et al.*, 2000; *Jewtoukoff et al.*, 2013] up to several thousand kilometers [*Sato*, 1993; *Preusse*, 2001; *Ern et al.*, 2011]. We will address this scale problem in section 3.

The analytical model of convective gravity waves assumes a three-layer atmosphere as shown in Figure 1. In the layer below z_b (bottom altitude of the convective forcing, typically a few kilometers above Earth's surface) and above z_t (top altitude of the convective forcing—between 8 km and 12 km depending on latitude) the background atmosphere remains unforced by diabatic processes. Latent heat release is restricted to the layer

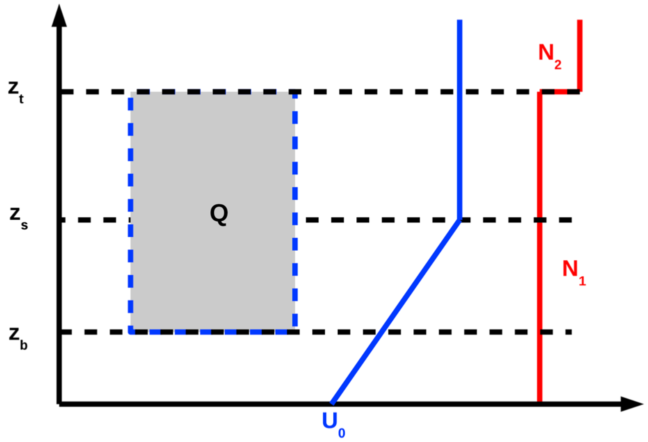

Figure 1. Schematic overview of the basic-state wind and stability profiles used in this study. The symbols z_b, z_t, and z_s represent the bottom and top altitudes of the diabatic forcing region Q and the shear level altitude. U_0 and U_t are background winds at the surface and the top level of the forcing. N_1 and N_2 are buoyancy frequencies with noncontinuous transition at the top of the forcing region.

between z_b and z_t. Further, a shear layer from the ground to some shear level z_s is assumed. Above this shear level the background wind profile is assumed to be constant with altitude and the buoyancy frequency has a noncontinuous transition from N_1 to N_2 at the top of the forcing region (see also *Beres et al.* [2004] and *Song and Chun* [2005] for further details on these assumptions). The momentum flux M for an arbitrary direction with angle ϕ counterclockwise to the zonal (eastward) direction can be calculated as

$$\bar{M}_\phi = \rho_0 \overline{u'_\phi w'} = \rho_0 \frac{1}{L_x L_y L_t} \int \int \int u'_\phi w' \mathrm{d}x\mathrm{d}y\mathrm{d}t \tag{1}$$

with ρ_0 as the density, u'_ϕ as the horizontal wind perturbation with respect to angle ϕ to the eastward direction, and w' as the vertical wind perturbation. The constants L_x, L_y, and L_t represent appropriate spatial and temporal grid sizes of the underlying atmospheric model. The momentum flux calculated by this model represents only GWs leaving the forcing region. Momentum fluxes inside the forcing region (e.g., storms) are mainly due to turbulence and are therefore neglected. After integration of equation (1), the momentum flux from the analytical model is obtained as

$$\bar{M}(c,\phi) = -\mathrm{sgn}\left(U_t - c\right) \rho_0 \frac{2(2\pi)^3}{L_x L_y L_t} \left(\frac{g}{c_p T_0 N_1^2}\right)^2 \frac{N_2}{|U_t - c|} |X|^2 \Theta(c,\phi) \tag{2}$$

Here U_t denotes the zonal background wind at cloud top altitude, c the GW phase speed, g the gravitational acceleration, T_0 the background temperature, c_p the heat capacity of air at constant pressure, and N_1 and N_2 the buoyancy frequencies at the location of the convective GW source with a noncontinuous transition at the top of the forcing (please refer to Figure 1 for further explanation). The parameter $|X|^2$ is called the wave filtering and resonance factor and represents the interference and superposition of waves internally propagating upward and downward between the borders of three model layers. This superposition leads to the characteristic shape [*Chun and Baik*, 1998; *Chun et al.*, 2001; *Song and Chun*, 2005; *Song et al.*, 2007] of the phase speed spectra at the top of the forcing region. $|X|^2$ is derived and discussed in more detail in *Song and Chun* [2005]. Equation (2) is the major result of the convective model and represents the momentum flux of convective GWs as a phase speed spectrum. It is noteworthy that *Beres et al.* [2004] followed a similar approach of convective GW source modeling. Differences are mainly found in the assumption of vertical distribution of the diabatic heating source. This, however, led to negligible deviations between both models as analyzed in *Beres et al.* [2004].

The diabatic heating source function $\Theta(c)$ assumes a forcing of Gaussian shape in space and time as derived in *Song and Chun* [2005]:

$$\Theta(c,\phi) = q_0^2 \left(\frac{\delta_h \delta_t}{32\pi^{3/2}}\right)^2 \frac{\sqrt{\pi/2}}{\sqrt{1 + \left(c - c_{qh}\right)^2 / c_0^2}} \tag{3}$$

Table 1. Spatial and Temporal Values for the Free Parameters of the Yonsei Convective GW Source Scheme[a]

Set	δ_h (km)	δ_t (min)
MF1	5	20
MF2	25	60
MF3	120	60

[a] MF1 and MF2 have been introduced in *Choi et al.* [2012]. MF3 is introduced in this work to account for large convective clusters (e.g., an ensemble of single convective cells distributed over a large region).

with $c_0 = \delta_h/\delta_t$ and δ_h, δ_t as the standard deviations of the spatial and temporal Gaussian and $c_{qh} (= c_{qx} \cos\phi + c_{qy} \sin\phi)$ as the moving speed of the convective system. Besides the tuning parameters δ_h, δ_t the initial propagation direction of each wave has to be defined. As in other studies before [*Choi et al.*, 2009, 2012], we carefully chose eight equally distributed launch angles in order to achieve a thorough angular sampling of the wavefield and also to be consistent with the additional GW background parametrization used. According to our sensitivity test, additional launch angles contribute little to the resulting momentum flux distributions while consuming precious computation time.

3. Implementation and Coupling With GROGRAT

The parameters δ_h and δ_t represent the spatial and temporal scales of the convection inside a certain model grid cell and largely influence the horizontal wavelength and periods of the excited waves. Different sets of parameters were used. Two parameter sets (MF1 and MF2; see Table 1) for the convective source have already been introduced in *Choi et al.* [2012]. MF1 has a prominent maximum in the momentum flux for waves of 10 km horizontal wavelength which is not visible to limb sounders. MF2 has been introduced for a better comparison with Atmospheric Infrared Sounder observational data. The peak in the horizontal wavelength spectrum was found at 50 km with a 15 times smaller intensity compared to MF1.

To represent convective GWs from large and long-lasting convective clusters as found prominently in the tropics [*Liu et al.*, 2015; *Khouider and Moncrieff*, 2015; *Kilpatrick and Xie*, 2015; *Trinh et al.*, 2016], we introduce another set of spatial and temporal scaling parameters—MF3. For this we chose a spatial scale of 120 km and an average forcing time scale of 60 min. As a consequence waves forced by this setup are more likely to be visible to limb-sounding instruments.

To calculate propagation and momentum flux of GWs from convection, the convective source model was used as the launch distribution for the GROGRAT ray tracer. The convective GW source model calculates a momentum flux spectrum as a function of phase speeds. Horizontal wavelengths are estimated according to *Choi et al.* [2012]

$$k_h = \frac{2\sqrt{\pi}}{\delta_h} \frac{1}{\sqrt{1 + \left(c - c_{qh}\right)^2 / c_0^2}} \tag{4}$$

Here δ_h is the spatial scale of the forcing, as defined above. The horizontal speed of the convection is given by c_{qh}. The characteristic velocity $c_0 = \delta_h/\delta_t$ is the ratio of spatial and temporal model constants.

The diagram in Figure 2 illustrates the coupling of source model and ray tracer. The source model uses heating profiles at every grid cell to calculate the convective forcing of GWs. Top and bottom of the forcing and an average forcing Q_0 are determined (cloud extent fitting) from these profiles with an initial guess from MERRA cloud data products. Initial cloud top data are obtained from MERRA itself. Cloud bottom data are obtained by descending the heating profile from cloud top downward to the first zero crossing. As a next step, cloud extent fitting is performed on the interval between both initial altitudes for cloud top and bottom. For performance improvements a shallow heating profile filter can be applied before the final profile fitting is performed. From these heating profiles momentum flux spectra are calculated by the convective GW scheme for different parameter setups (indicated by MF-1..MF-X).

As a next step a peak analysis is performed to find the dominant modes to be ray traced in the momentum flux spectra from the convective GW source model. The reason is that GROGRAT computes trajectories for single waves with discrete phase speeds, horizontal wavelengths, and amplitudes. The phase speeds determined by the peak analysis are further considered for the calculation of the horizontal wavelength. The horizontal wind

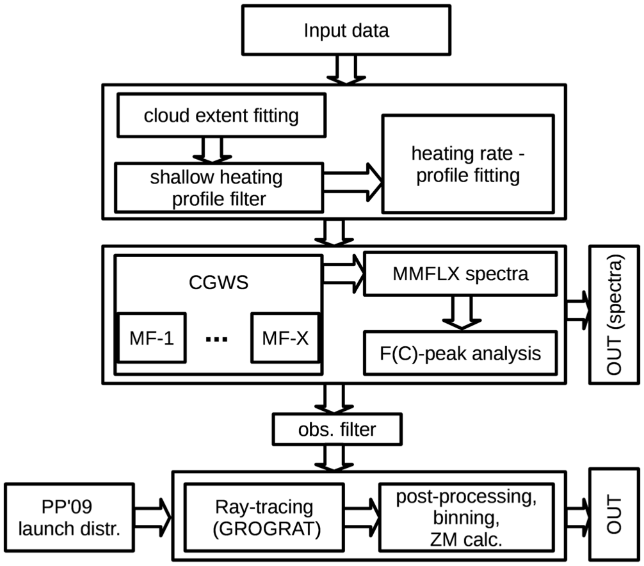

Figure 2. Coupled convective GW source model and GROGRAT ray tracer. From top to bottom: input data set (MERRA data were used for this study) provides winds, temperature, geopotential, heating rates, and cloud top height. Two preparative steps (cloud extent fitting and shallow heat profile filter) are performed to calculate the correct bottom and top of the heating source and to filter out shallow clouds. The resulting heating source characteristics serve as an input for the convective GW source model. The GROGRAT ray tracer utilizes the output data of the source as GW characteristics together with the background atmosphere to calculate GW trajectories. Additionally, an observational filter and background parametrization can be comprised into the simulation. As a last step the usual statistical binning and analysis is applied to obtain derived quantities like GW drag and squared temperature amplitudes. For further details see text.

amplitude $\hat{u}$ of the wave can now be obtained by the following equation valid in midfrequency approximation (this equation is based on the polarization relations [*Ern et al.*, 2004]):

$$\hat{u} = \sqrt{\frac{m}{k_h}\frac{2M_\phi}{\rho}} \tag{5}$$

with k_h and m as the horizontal and vertical wave number and M_ϕ denotes the momentum flux in direction ϕ. With this input data GROGRAT simulations can be performed for each individual wave found in the peak analysis of the convective source model output. The postprocessing of GROGRAT data is similar to the method in *Preusse et al.* [2006, 2009]. GW drag and amplitude are calculated for a regular grid. Additionally, possible contributions to the momentum flux distribution from other sources than convection were also considered in order to compare the simulation results with observations (see section 7). For this reason, our convective GW ray tracing model can be augmented with a momentum flux background for higher latitudes. This background scheme mainly influences the momentum flux at high latitudes for the following reasons.

The high amount of GWs from convective sources in low latitudes yields a much higher weight of convective waves compared to the background parametrization. At higher latitudes, however, convective GWs are outnumbered by background waves (see Figure A1). Therefore, middle- to high-latitude momentum flux is prominently induced by background waves. Another issue to consider when comparing simulations with observations is the spectral visibility of convective GWs to limb-sounding instruments. GWs generated by the Yonsei convective source scheme may have, depending on the choice of δ_h and δ_t, very short horizontal wavelengths which are consistent with the concept of subgrid-scale GWs but unlikely to be resolved by limb-sounding instruments like SABER and High Resolution Dynamics Limb Sounder (HIRDLS).

4. Limb-Sounding of Gravity Waves and Its Limitations

The SABER instrument observes atmospheric infrared emissions in the 1.27 μm to 16.9 μm band, subdivided into 10 channels. Measurements are performed in limb-sounding geometry. Atmospheric temperatures can be derived from observed limb radiances from the tropopause region to well above 100 km altitude with a vertical field of view of 2 km. The limb measurement geometry implies some limitations in the observation of wave-like features with a sensitivity depending on the horizontal and vertical wavelengths of the respective wave. The corresponding sensitivity or visibility function accounts for the efficiency in wave detection [*Preusse et al.*, 2002].

We use our coupled model of convective GW source parametrization and GROGRAT ray tracer to assess the instrument's limitations due to the limb-sounding measurement geometry. For this purpose, the analysis of the ray tracing results has been extended by a simple approach sorting out GWs which cannot be observed by SABER. A simple restriction of 100 km for the lowest observable horizontal wavelength is applied according to *Ern et al.* [2004]. Only waves which can pass the observational filter are considered in the later calculations and binning process. This will affect the majority of GWs excited in the original MF1 setup of the convective source model [*Trinh et al.*, 2015a]. The MF2 setup adds some more longer waves within the horizontal wavelength range of approximately 80 km. The third setup, MF3, adds waves which can pass this simple observational filter but still carry less momentum flux. For obtaining a more realistic distribution and amount of momentum flux, a combined setup of MF1, MF2, and MF3 is used for the GW source in order to simulate the observations from the SABER satellite in tropical regions. For global comparisons, a GW background parametrization [*Preusse et al.*, 2009] was added for the representation of high-latitude GW sources. The advantage of this particular parametrization is that it also uses GROGRAT to calculate three-dimensional propagation of GWs. The combination of our convective ray tracing scheme and the *Preusse et al.* [2009] scheme results in a self-consistent model. Both models differ only in terms of the launch distribution. In the case of *Preusse et al.* [2009], the launch distribution was chosen to best fit observational data. It is noteworthy to mention that other state-of-the-art parametrizations exist [e.g., *Yiğit et al.*, 2008]. However, these parametrizations are limited to vertical-only propagation. As found in *Kalisch et al.* [2014], differences between three-dimensional and vertical-only propagation are significant hence our choice for a background parametrization from GW ray tracing.

The results of the composite GW momentum flux distribution are discussed in section 7. Further analysis of a larger selection of composite setups can be found in *Trinh et al.* [2016]. In contrast to our study presented here, *Trinh et al.* [2016] focus on GWs which can be observed by limb-sounding satellites and infer relevant spatial and temporal scales.

5. Results Without Observational Filter

For the following investigations on convective GWs the MERRA data set [*Rienecker et al.*, 2011] served as source for profiles of heating rates. For consistency, atmospheric background data of wind, temperature, and geopotential height were also taken from the same data set. MERRA data include several ground-based, in situ, and satellite measurements through 3DVAR assimilation into the Goddard Earth Observing System (GEOS) [*Suarez et al.*, 2008]. It provides a horizontal resolution of $^1/_2$° longitudinal and $^2/_3$° latitudinal with 72 levels up to 70 km with assimilated satellite data up to the mesosphere. Several studies proofed the reliability of this record [*Bosilovich et al.*, 2011] (first MERRA data are available for 1979 and already implemented the very first satellite observations of the middle atmosphere. Further information can be obtained from http://disc.sci.gsfc.nasa.gov/daac-bin/DataHoldings.pl.) especially for precipitation and heating rates. This is important because the Yonsei convective scheme requires heating rate profiles and their analysis in terms of bottom, top, and maximum heating. Please note that the diabatic heating rate provided by MERRA is deep convective heating and pure model output without assimilated observations. Consequentially, MERRA deep convective heating rates solely depend on the cumulus parametrization of MERRA's GEOS-5 atmospheric data assimilation system. Similar, however, is also true for other reanalysis data.

Figure 3a shows MERRA heating rates obtained by averaging over the whole heating rate profile and time averaged for January 2008. High values of about 4 K/d are found over the Pacific Ocean. Also, South America, the southern part of Africa, and Madagascar as well as the West Pacific region show higher heating rates around 2–3.5 K/d. These are the characteristic regions for strong convection with high amounts of precipitation and evaporation. Another feature are the higher values along the Intertropical Convergence Zone (ITCZ) in the Pacific and Atlantic Oceans close to the equator. In July 2008 regions with highest heating rates are found in the Northern Hemisphere (Figure 3c). Highest values about 5 K/d are found in India and Indochina and also in Central America. Heating rates over Africa are lower (2.5 K/d) but still a pronounced feature. All these regions show higher GW momentum flux, because latent heat release is a major factor in the forcing of convective GWs with its subsequent release of GW momentum flux. The global distribution of the diabatic heating rate provided by MERRA is generally similar to observed global precipitation data from the Global Precipitation Climatology Project [*Adler et al.*, 2003] (not shown here).

Figures 3b and 3d show momentum flux at cloud top height for average January and July 2008 conditions. Momentum flux at cloud top height is correlated to average heating rates from Figures 3a and 3c. The depth of the heating is another major factor influencing the momentum flux distributions at cloud top height. For this reason, the Pacific and continental regions show remarkable momentum flux forcing. Also, the Indian Ocean region is another strong source of convective GWs. However, the large regions of shallow clouds (flagged white due to the shallow cloud filter in Figures 3b and 3d) do not excite convective GWs.

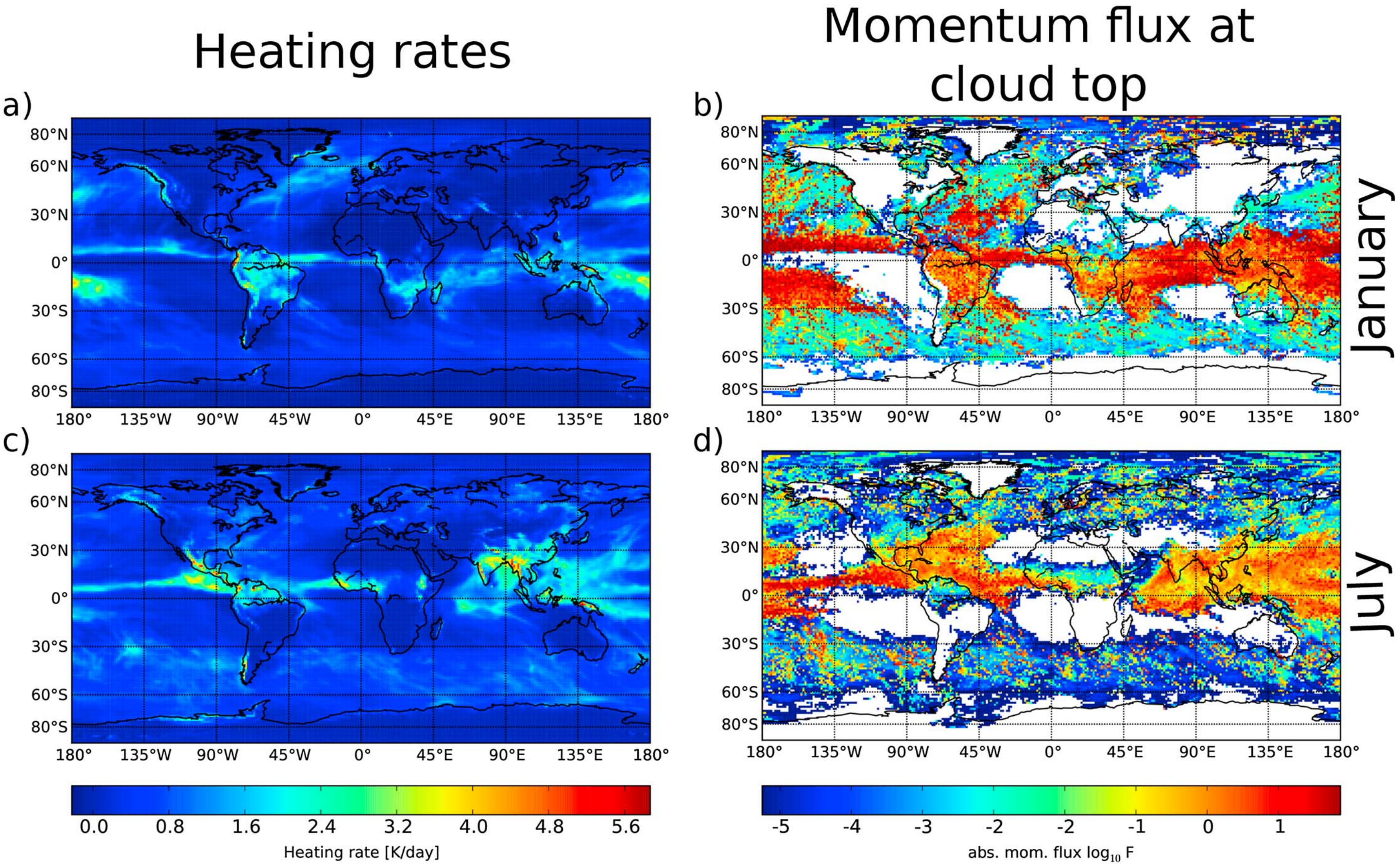

Figure 3. (a and c) Heating rates from MERRA data and (b and d) momentum flux at cloud top height from convective GW source scheme for January and July 2008.

Figures 3b and 3d show a typical seasonal distribution of momentum flux at cloud top height. The main forcing regions in the tropics follow well the ITCZ and are found in the Southern Hemisphere during January 2008 and in the Northern Hemisphere during July 2008. Further, the excitation is enhanced above the continents due to the known deep convection above the rain forests. Most notably, the Asian monsoon region shows strong momentum flux values at source level. Previous studies [*McLandress et al.*, 2000; *Preusse et al.*, 2001; *Jiang et al.*, 2004; *Preusse and Ern*, 2005; *Jia et al.*, 2014] associated observed higher momentum fluxes found in the tropics with increased convective GW activity. Nevertheless, strong convection can be found at higher latitudes as well. Besides deep convection in the subtropics, tropical cyclones and midlatitude storms are other major sources of GW momentum flux due to deep convection which has already been subject of study [*Kim et al.*, 2005, 2009; *Lehmann et al.*, 2012]. In addition, *Preusse and Ern* [2005] and *Jia et al.* [2014] found evidence for convective GWs above warm ocean currents, e.g., the Gulf Stream and the Kuroshio.

In a next step we want to constrain the two free parameters of the convective GW source model by comparing modeled distributions of momentum flux to global observations. Uncertainties of these observations are discussed in section 6 where we address the limitations of limb-sounding satellite observations.

Three sets of parameters are applied to the convective source model to best fit the simulated global momentum flux distributions to satellite observations. Previous studies [*Choi et al.* 2009, 2012] indicate a demand for such a further tuning of the source model to resemble satellite observations. Because different instruments are sensitive to different parts of the GW spectrum, the location of the observed spectral peak in the spectral domain can vary considerably [*Choi et al.* 2009, 2012; *Ern and Preusse*, 2012]. Therefore, a single set of model parameters is likely not sufficient. How do the free parameters of the convective GW source model influence the spectrum of the excited waves? To answer this question, we performed simulations for all three parameter sets in Table 1.

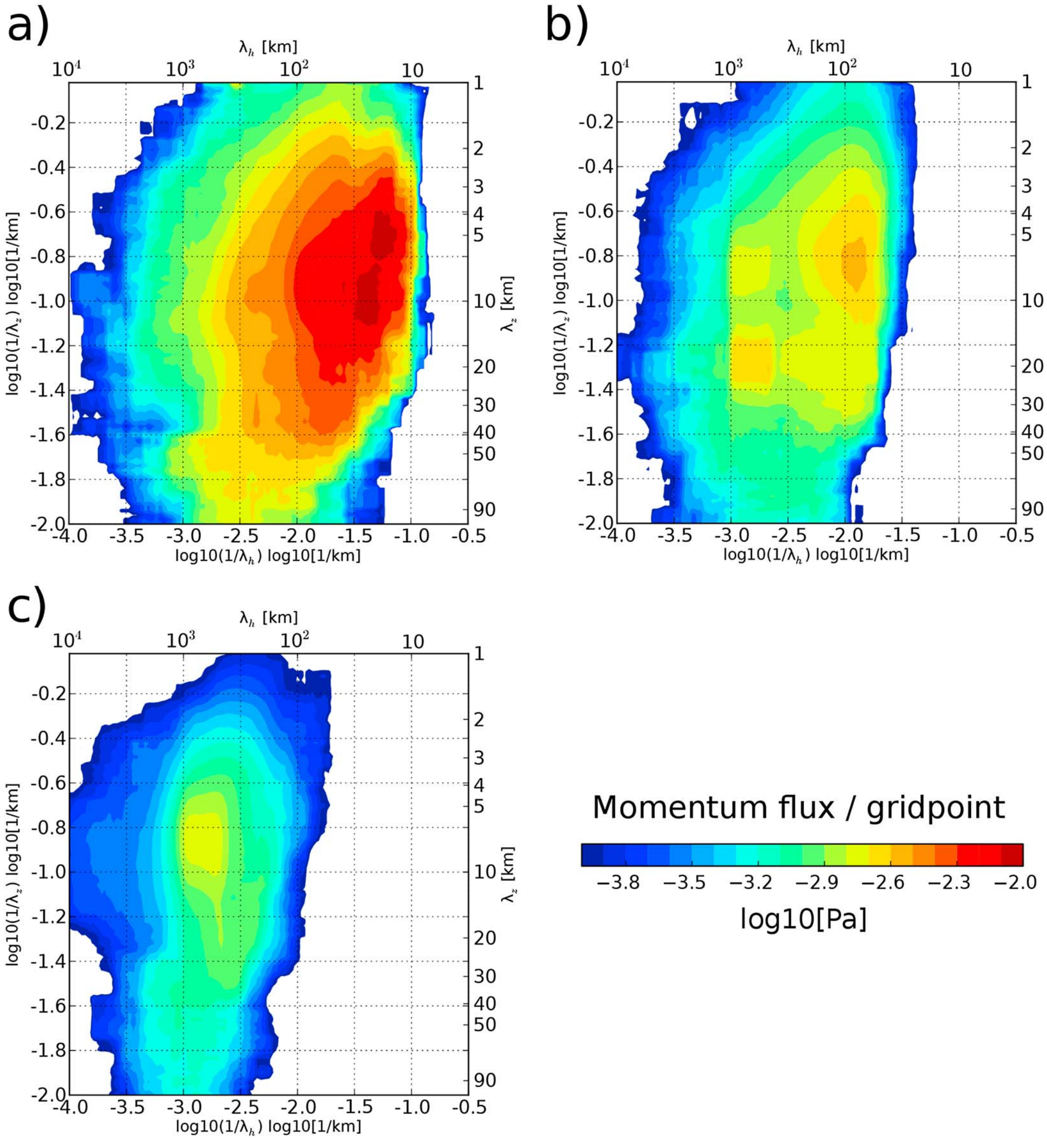

Figure 4. Momentum flux per grid point as a function of horizontal and vertical wavelengths for (a) MF1, (b) MF2, and (c) MF3 parameter sets at 25 km altitude for January 2008 conditions.

The momentum flux results after ray tracing are shown in Figure 4 as a function of horizontal and vertical wave number at 25 km altitude for January 2008. The spectrum was calculated by binning momentum flux values from single waves with respect to their horizontal wave number $k_h = 2\pi/\lambda_h$ and vertical wave number $m = 2\pi/\lambda_z$ in logarithmic coordinates $\tilde{k}_h = \log_{10}(\lambda_h^{-1})$ and $\tilde{m} = \log_{10}(\lambda_z^{-1})$ with grid spacings of $\delta\tilde{k}_h = 0.1$ and $\delta\tilde{m} = 0.1$ and an overlap of $\Delta\tilde{k}_h, \tilde{m} = 0.2$. Momentum flux values are summarized separately for each bin and normalized with respect to the average momentum flux found at that particular altitude. The central peak of the MF1 parameter set ($\delta_h = 5$ km, $\delta_t = 20$ min , Figure 4a) is obtained at approximately 15 km horizontal wavelength and 10 km vertical wavelength. This is in good agreement with findings from *Choi et al.* [2012] where a peak horizontal wavelength of 10 km was reported. Deviations to results presented here may arise from different ray tracing models used. For instance, in *Choi et al.* [2012] and *Choi et al.* [2009] the GW ray tracer from *Song and Chun* [2008] was used for propagation and amplitude calculation of the GWs. The result of the second parameter set (MF2, $\delta_h = 25$ km, $\delta_t = 60$ min) is presented in Figure 4b. The maximum momentum flux per grid point is now obtained at approximately 90 km horizontal wavelength and 7 km vertical wavelength. The maximum momentum flux is decreased by half an order of magnitude compared to Figure 4b. Albeit the spectral distribution is shifted to longer horizontal wavelengths, the majority of the momentum flux caused by MF2 is still not visible to an instrument like SABER which has a low likelihood for observing GWs with horizontal wavelengths shorter than 100 km. This limitation, however, is due to the limb-observing geometry of the SABER system and not the result of any detector constraints [see, e.g., *Preusse et al.*, 2006].

The MF3 parameter set ($\delta_h = 120$ km, $\delta_t = 60$ min) to account for large-scale convective clusters shows different spectral characteristics. Its temporal scale is the same as for MF2, and only the spatial parameter is shifted toward longer scales to account for even larger convective events than MF2. The result is shown in Figure 4c. The maximum average momentum flux is approximately 1.6 mPa (i.e., −2.8 in log units) and found at 700 km horizontal wavelength and 5.5 km vertical wavelength. The whole horizontal spectrum of MF3 consists of waves with horizontal wavelengths longer than 100 km and is therefore observable by a limb-sounding instrument. The location of this maximum is partly determined by the wave resonance and interference factor X^2 [*Song and Chun*, 2005] which itself is the result of the vertical structure of the convective forcing region. This factor directly shapes the phase speed spectrum in terms of single peaks which are easy to identify as an input for the ray tracer. And the horizontal and vertical wavelengths can be easily determined from the dispersion relation. The phase speed of each particular wave is relevant for the filtering of GWs. This is particularly important for GWs excited in the ITCZ regions. Those waves are filtered out already close to their source. In that case, the slow phase speeds lead to filtering within the troposphere with comparable slow wind speeds.

To further complete the picture of convective GWs, all three simulation runs have been superimposed to one composite result:

$$\mathrm{MF}_{\mathrm{comb./Bin}} = \mathrm{MF1} + \mathrm{MF2} + \mathrm{MF3} \tag{6}$$

where MF may denote momentum flux, drag, or temperature amplitudes. As a first attempt and for simplicity we avoid the introduction of additional weighting factors in equation (6). Still, we like to emphasize the opportunity to do so to account for different relative forcing efficiency between these three parameter sets.

Figure 5 gives an overview of average momentum flux (a and b), GW drag (c and d), and temperature amplitude (e and f) for January 2008 (a, c, and e) and July 2008 (b, d, and f). The discussed values are presented in color. Additionally, the background winds are plotted as contours. The momentum flux (logarithmic scale) shows a strong decay in amplitude from lower altitudes to higher altitudes. This decay is in good agreement with the filtering of GW. As an example, waves in the winter hemisphere can propagate to higher altitudes due to a gain in amplitude which is possible for waves propagating against the winter hemisphere jet [*Ern et al.*, 2015]. Especially, GWs in the Southern Hemisphere midlatitudes of July 2008 propagate up to 50 km altitude where they are filtered out.

Relatively high GW drag (Figures 5c and 5d) with accelerations of 16 m/s/d in the upper stratosphere to lower mesosphere region is found in this combined simulation. Also, the direction of the GW drag changes as the dominant wind direction changes (zero crossing in wind). Previous studies [*Ern et al.*, 2014] report a derived stratospheric (<40 km) GW drag of less than 1 m/s/d with an error margin of factor 2–3. Also, *Ern et al.* [2013] found GW drag values of up to 5 m/s/d at 60 km altitude—again with an error margin of factor 2–3. This means that the values obtained in our study are somewhat higher but qualitatively in reasonable agreement. Somewhat higher values are expected because our simulation includes also waves invisible to SABER. Also, small deviations in the distribution of momentum flux , temperature amplitudes, and GW drag are expected because of the absence of GW sources other than convection (e.g., GWs from jet instabilities and orography). Important effects like the relative efficiency of different GW sources and wave-wave interaction [*Medvedev and Klaassen*, 2000; *Yiğit et al.*, 2008; *Lund and Fritts*, 2012] were neglected in our simulation. The temperature amplitudes of high-latitude waves in Figure 5 remain high, even though the number of convective waves propagating to these latitudes is very low compared to tropical regions. Therefore, momentum flux, GW drag, and squared temperature amplitude values of the extratropics should be carefully interpreted. Only a smaller number of GWs propagate to higher latitudes, and hence, the statistical sampling of momentum flux per bin is not reliable for these regions.

Figure 6 shows maps of GW absolute momentum flux of unfiltered results (a–f) and for filtered (horizontal cutoff wavelength of 100 km) results (g–l) at 25 km, 35 km, and 45 km altitude in the tropics for January (a–c and g–i) and July (d–f and j–l) 2008. The momentum flux at different altitudes shows some similar features to the momentum flux at cloud top height (Figures 3b and 3d). The deep convection source indicates

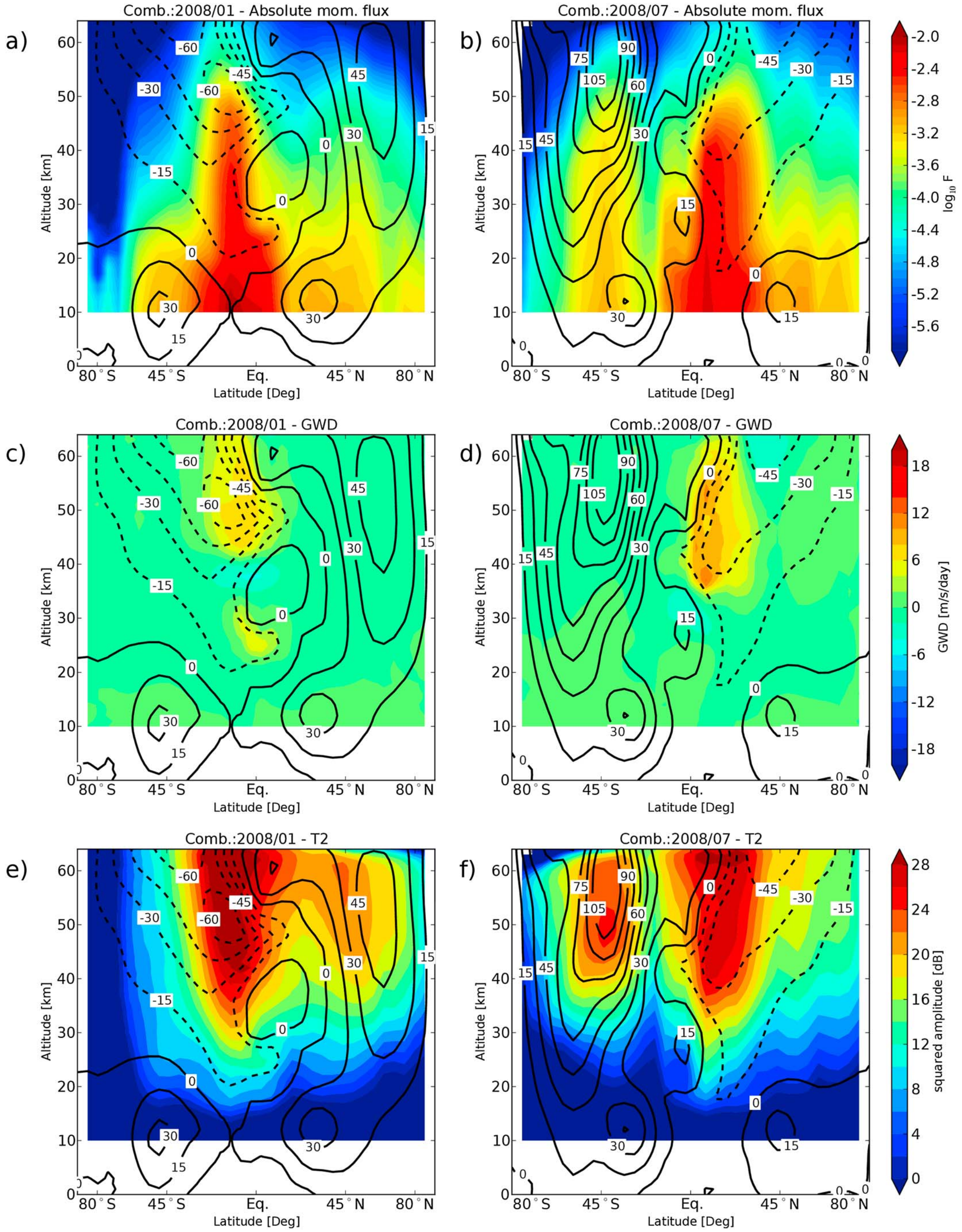

Figure 5. Zonal averages for the combined setup of (a and b) momentum flux, (c and d) GW drag, and (e and f) temperature amplitudes for January 2008 conditions (Figures 5a, 5c, and 5e) and July 2008 conditions (Figures 5b, 5d, and 5f). For more details see text.

a higher activity above continents. However, there are differences above the oceans where high momentum flux values are found at source level (Figures 3b and 3d). The ray tracing results show much lower momentum flux in these regions even at altitudes as low as 25 km in Figure 6. For example, the eastern Pacific region, the South Atlantic Ocean, and the South Indian Ocean west of Australia show lower momentum flux values. In these regions the depth of the heating is too shallow to generate GWs which are not wind filtered directly above the source. For January conditions maximum momentum flux due to convective GWs is found over central South America, South Africa, and Indonesia between 5°S and 10°S. For July, the regions of maximum

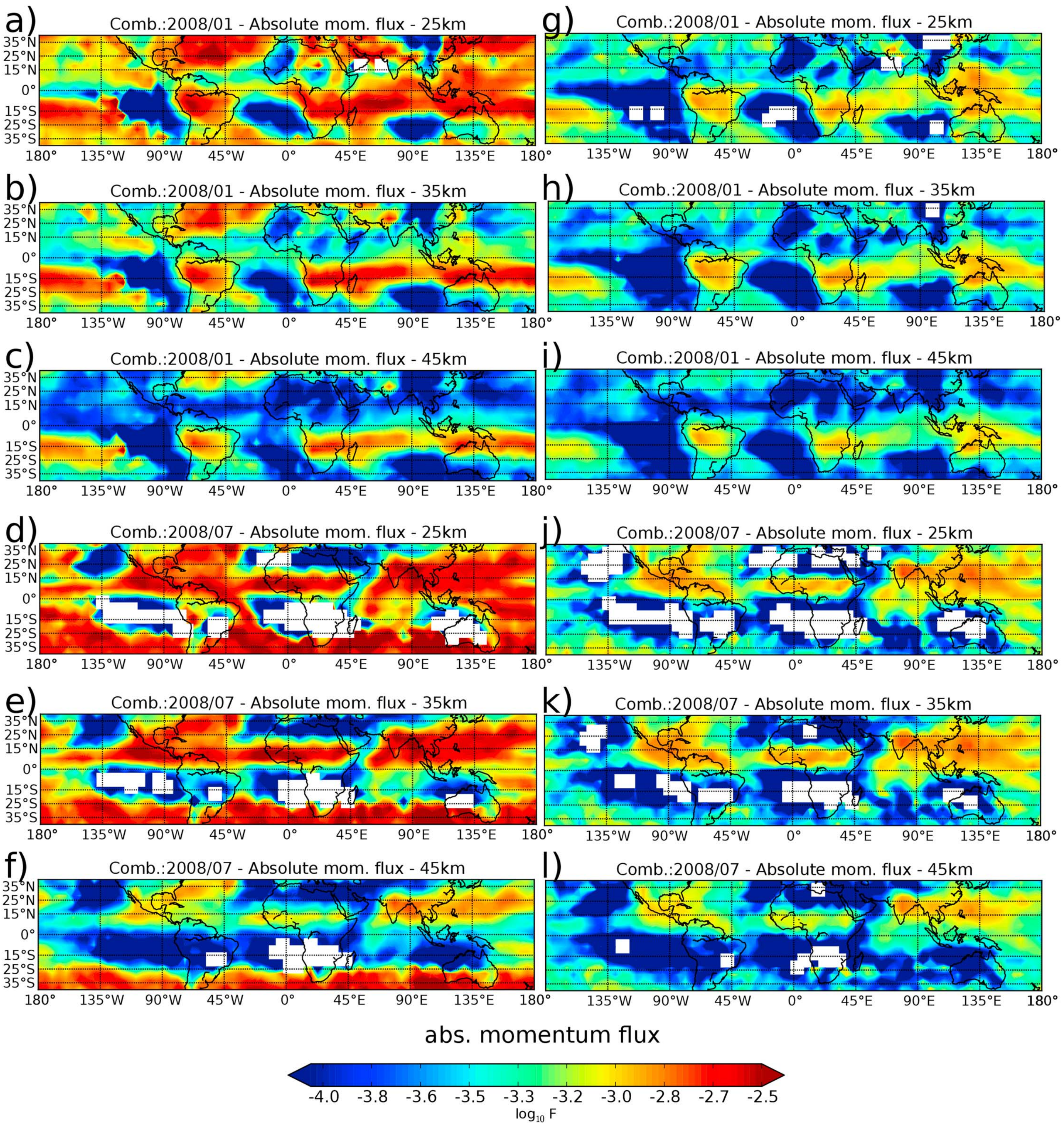

Figure 6. Absolute momentum flux from simulated convective gravity waves (superimposed setup for MF1–MF3) at altitudes 25 km, 35 km, and 45 km for (a–c and g–i) January 2008 and (d–f and j–l) July 2008. Figures 6a–6f show unfiltered results, and Figures 6g–6l show results with a horizontal wavelength cutoff at 100 km.

momentum fluxes are found northward shifted at latitudes between 5°N and 10°N due to the seasonal cycle (for July conditions see Figures 6d–6f and 6j–6l).

Still, these results represent convective GWs only. Neither waves from other specific sources nor waves from a general background launch distribution are taken into account. For that reason, these isolated convective wave momentum fluxes are higher than expected but may probably decrease in a GW simulation accounting for additional sources because these high values may be downweighted by adding lower MF waves from sources other than convection.

6. Impact of Observational Filter

To account for observational limitations of SABER satellite measurements, we introduce a simple observational filter. This raises the following question: How do observational limitations of limb-sounding instruments affect the momentum flux distribution? A direct comparison of filtered and unfiltered simulation data will answer this question. For this, we enhanced our model by including a filter step to account for the low visibility of short horizontal GWs. Simplicity is advantageous in terms of computational efficiency since this filter has to be applied on every single GW trajectory. The coupling between the source model and the GROGRAT ray tracer is similar to our previous work in this paper and only extended in terms of the additional observational filter to investigate the importance of this effect for the observation of convective GWs by a limb-sounding instrument like SABER. For this reason, the convective GW source scheme was utilized with the same combined parameter setup from the last section. Figure 6 shows global maps of absolute momentum flux (GW estimation from SABER temperature variances does not allow the retrieval of the horizontal wave vector. Therefore, only absolute horizontal wavelengths can be estimated and used to calculate the absolute momentum flux according to *Ern et al.* [2004]. For better comparison, the ray tracing data are also analyzed with respect to absolute values.) from simulation which can be compared to the corresponding results from SABER observations (Figure 7). Both figures show January 2008 conditions in the left panels and July conditions in the right panels for altitudes from 25 km to 45 km. The simulated structures with observational filter of Figures 6g–6l are qualitatively in good agreement with the results of Figures 6a–6f. The convective source is strongest above the continents and lowest west of South America, Africa, and Australia due to smaller vertical extent of convection in this region. Despite the generally lower momentum flux in Figures 6g–6l, the altitude dependence is much weaker compared to Figures 6a–6f.

Waves potentially visible to SABER propagate almost conservatively up to the middle stratosphere. Also, the decline of momentum flux with altitude is reduced in the ray tracing results compared to SABER observations. This indicates that the amplitude saturation limit was still not reached for most of the simulated waves at altitudes lower than 45 km. The SABER observations on the other hand show strong dissipation with altitude (Figure 7). It is noteworthy that these observational results include waves from other sources besides convective GWs. Further, SABER momentum fluxes at 25km are somewhat high biased due to increased noise at low altitudes [see also *Jia et al.*, 2014]. Overall, however, values of the simulated GW momentum flux match well in their order of magnitude.

Another feature found is the seasonal cycle of the SABER results with the south to north shift of the continental momentum flux maxima between January and July conditions. The Asian monsoon region shows one of the strongest peaks at 25 km altitude and is also a prominent feature of the simulation. Still, GWs from the Asian monsoon region may be slightly overpronounced in the simulation. Higher momentum flux values are found over larger areas of the Pacific Ocean. This feature is maintained throughout the vertical propagation of the waves and is therefore also found at 45 km altitude. SABER results show lower momentum flux values at this altitude. Zonal average momentum fluxes from simulation including observational filter (Figures 8a and 8b) show indeed an increased momentum flux at 10°N/S at altitudes as high as 50 km in January and 45 km in July. GW amplitudes become large, and waves saturate at the top of the maxima at 40–50 km. This results in a strong decrease in momentum flux. Only small net drag is exerted where eastward and westward propagating waves saturate and their drag in both directions largely compensates [*Trinh et al.*, 2016]. Some preference in the propagation direction causes drag in the order of 1-2 m/s/d in the absence of vertical wind gradients. However, in the presence of vertical wind gradients some GWs are refracted to lower vertical wavelengths. This causes saturation, and subsequently, larger drag is exerted. This implies that the remaining GWs (after application of an observational filter) are fast waves. Hence, they can propagate to the upper stratosphere/lower mesosphere region. Consequently, the GW drag is generally lower. Maxima are prominently found within the tropics. The largest differences to the nonfiltered run can be obtained in the temperature amplitudes

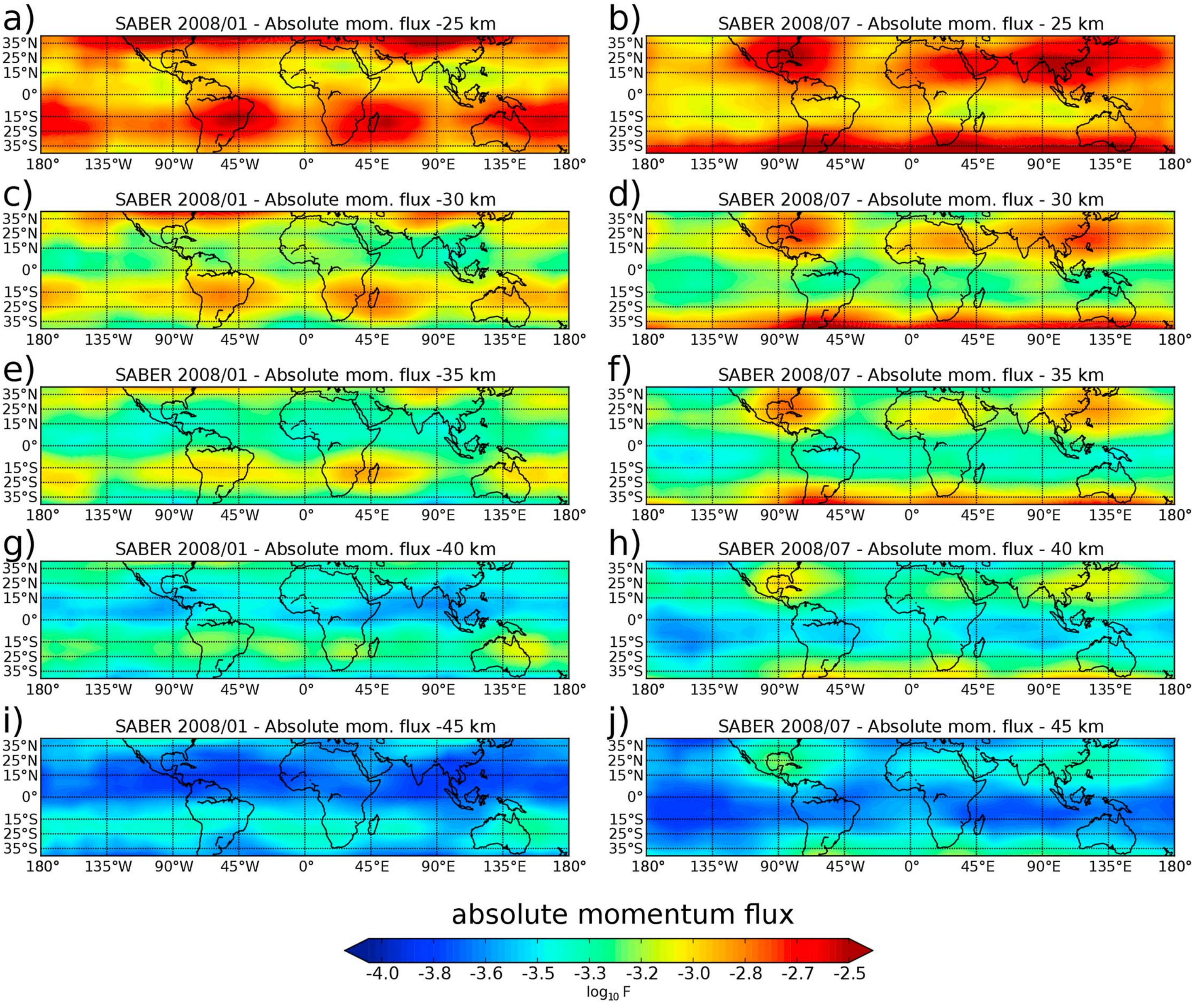

Figure 7. GW momentum flux derived from the SABER satellite instrument for (a, c, e, g, and i) January 2008 and (b, d, f, h, and j) July 2008.

(Figures 8e and 8f). The maximum amplitudes (up to 28 dB) are found at altitudes of 55 km and above. Please note that these values are the result of only convective GW forcing and therefore much higher than observable GW temperature amplitudes. Considerable lower amplitudes are found in the background wind reversal at 40 km (<12 dB). The extratropical temperature amplitudes are increased compared to Figure 5.

7. Comparison of Global GW Ray Tracing and Satellite Data

Even though encouraging results were found for low-latitude regions, modeling of higher latitudes is also needed for a comparison on a global scale. For that purpose, waves from the *Preusse et al.* [2009] GW launch spectrum were added to the convective GWs. This combination of both launch distributions was done by a weighted average:

$$F = \frac{1}{\epsilon N_{\mathrm{bkgd}} + N_{\mathrm{CGW}}} \left(\sum_{i=1}^{N_{\mathrm{bkgd}}} \epsilon F_{\mathrm{bkgd},i} + \sum_{i=1}^{N_{\mathrm{CGW}}} F_{\mathrm{CGW},i} \right) \tag{7}$$

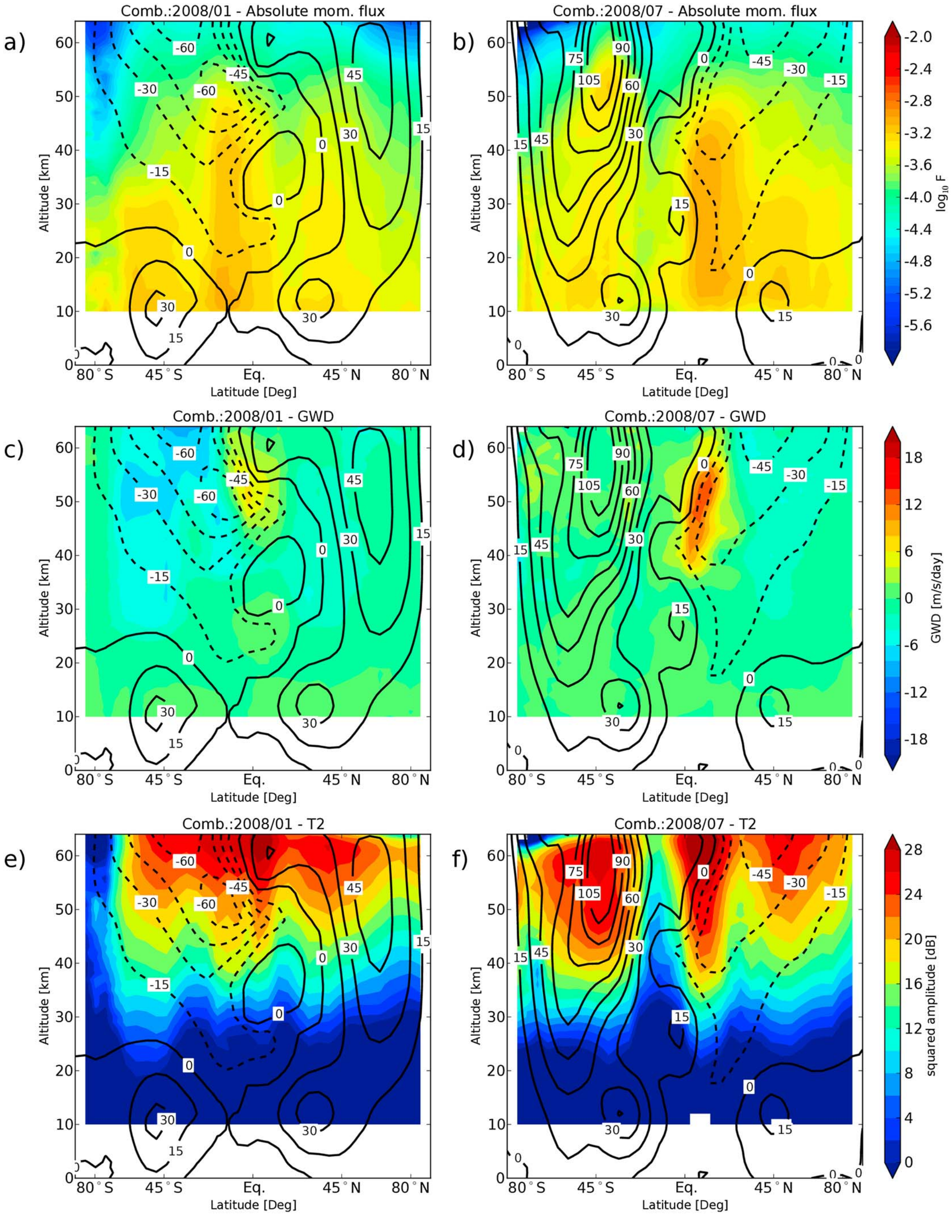

Figure 8. Combined zonal averages of (a and b) momentum flux, (c and d) acceleration, and (e and f) temperature amplitude with visibility filter. Please note that intermittency with other GWs sources was not taken into account. Thus, simulated amplitudes are upper limits.

F is the overall momentum flux of the combined model. F_{bkgd} and F_{CGW} are momentum flux values for the background GW spectrum (bkgd) and the convective GWs (CGW). N_{bkgd} and N_{CGW} denote the number of each kind of waves within one spatial bin. The background spectrum also represents waves from convective sources. These GWs have to be neglected in the combination of background and convective GW; hence, the factor ϵ is introduced. We chose to set $\epsilon = 0.1$. Due to this factor, convective GWs dominate low-latitude regions and reduce the momentum flux per bin in high-latitude regions. If there are regions without CGWs, ϵ cancels out, and the MF values originate from the *Preusse et al.* [2009] background alone.

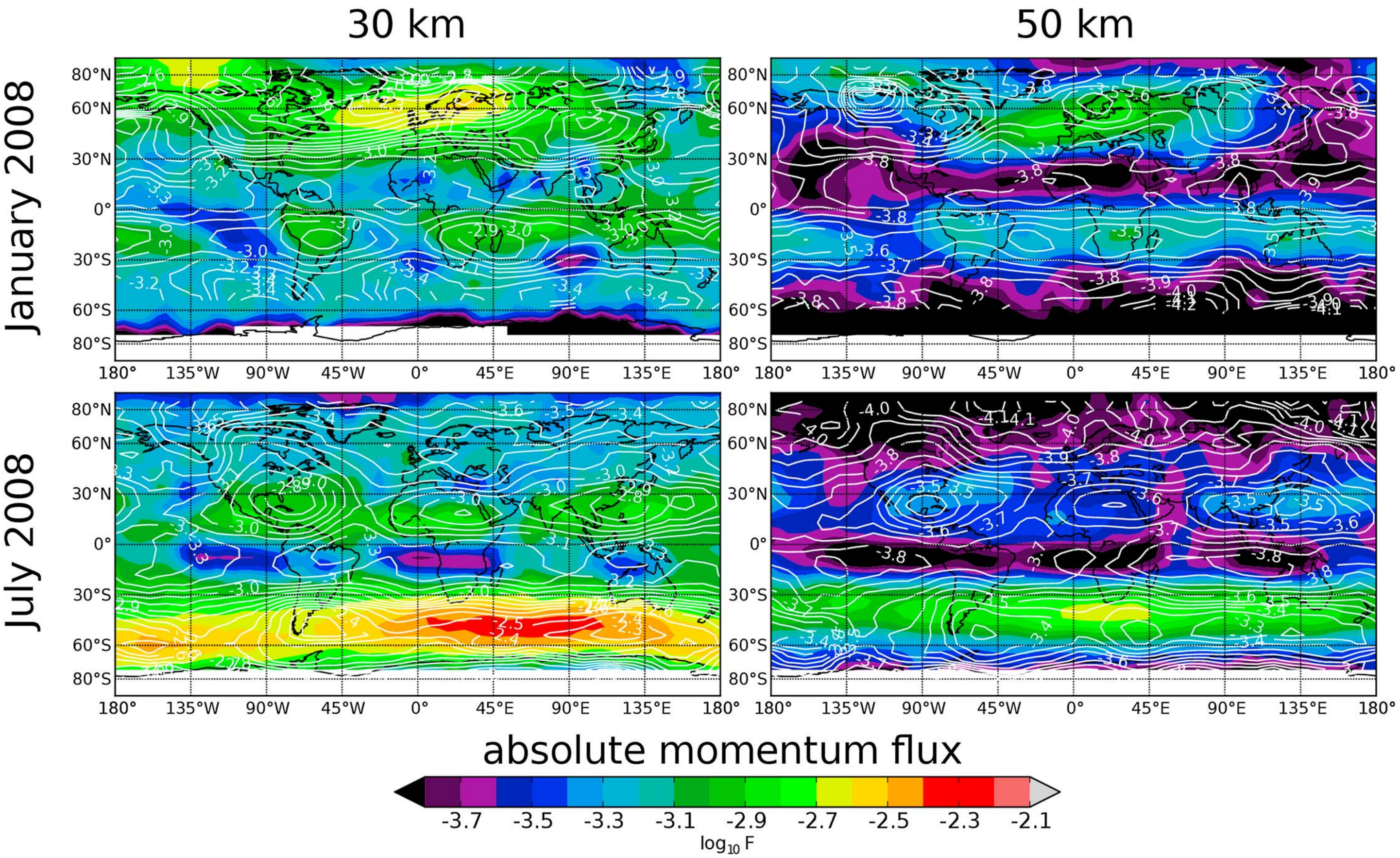

Figure 9. Combination of MF1–MF3 parameter setups with visibility filter (GWs shorter than 100 km have been filtered out). A background parametrization after *Preusse et al.* [2009] was added for better comparison with SABER satellite measurements (white contour lines).

Figure 9 shows the resulting momentum flux distribution for the ray tracing of both launch distributions combined (color) and SABER satellite data (contour) for a direct comparison for January 2008 (top row) and July 2008 (bottom row). Figure 9 (left column) shows results for 30 km altitude, and Figure 9 (right column) shows results for 50 km altitude. Compared with the results in section 6, Figure 9 shows a better agreement with SABER observational data in terms of location of local maxima/minima of momentum flux and its absolute value. The momentum flux between 30°S and 30°N is dominated by the ray tracing calculation of convective GWs from all three convective source setups combined including the visibility filter.

In contrast, momentum flux values at higher latitudes originate predominantly from the background GW spectrum after *Preusse et al.* [2009] (also see Appendix 1). Compared to the simulations by *Preusse et al.* [2009], in particular, the tropical peaks above the continents are better resolved. The South American momentum flux maximum is found above the Amazonian Rainforest in the simulation and in observational data for January conditions. The peak over Madagascar as seen in the SABER observations spans from South Africa to the Indian Ocean. Also, the high momentum fluxes above Indochina found by SABER are well represented in the simulation. Further, localized minima like in the observations, but with somewhat lower momentum flux values than in the observations, are found in the tropics of the winter hemisphere. Comparing SABER measurements and GW simulations for 50 km altitude, the general latitudinal structures are in good agreement. The maxima in momentum flux compare well to the observation (SABER) in position and value for January and July.

Since both source parametrizations do not include any orographic GWs, the typical momentum flux maximum at, e.g., the Drake Passage is not represented in the simulation. Despite these typical mountain wave regions, the overall agreement in structure and absolute values between observation and simulation is encouraging.

Figures 10a and 10b show the zonal mean absolute momentum flux of the combined convective and background parametrization in color. SABER measurements of momentum flux are indicated as contour lines

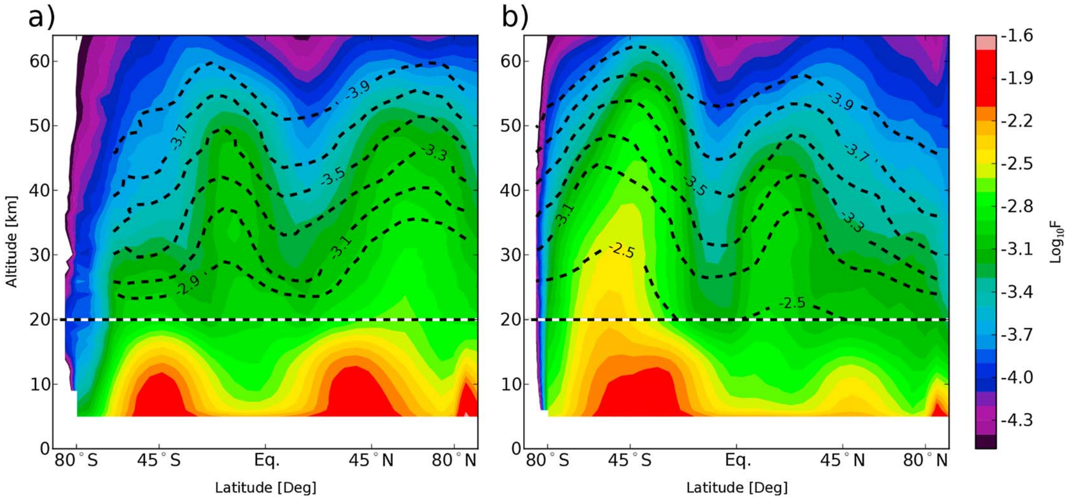

Figure 10. Momentum flux zonal averages of the combined simulation MF1–MF3 with visibility filter (color) and the *Preusse et al.* [2009] GW parametrization as background for (a) January 2008 and (b) July 2008. SABER measurements are indicated as contour lines. Error margin of SABER is about 0.3 order of magnitude of momentum flux.

starting at 20 km altitude. In the troposphere maxima are found at approximately 45°N/S with a steep decay rate. Momentum flux already decreased about 1 order of magnitude at 20 km altitude. In the stratosphere (Figure 10a) the Northern Hemisphere (winter) maximum in momentum flux is found between 45°N and 80°N with logarithmic momentum flux values of about −2.8 (1.6 mPa) at 20 km to −3.3 (0.5 mPa) at 50 km altitude. This is in very good agreement with the SABER data (error margin of SABER is about 0.3 order of magnitude) in terms of structure and order of magnitude. The Southern Hemisphere (summer) peak is found around 15°S in the stratosphere for the ray tracing calculations and is found to be northward shifted by more than 5° compared to SABER measurements. Still, the vertical decay in momentum flux is found consistent with the decay of the observed GW momentum flux. Similar agreement is found in Figure 10b for July conditions during Northern Hemisphere summer/Southern Hemisphere winter.

8. Summary

In this study we presented results from simulations using the GROGRAT GW ray tracer and the Yonsei convective GW source model. For this purpose, both models have been coupled with each other. Momentum flux calculations at cloud top height from the convective GW source model showed a characteristic seasonal behavior with a hemispheric shift in heating rate distributions following the ITCZ and land precipitation patterns (e.g., monsoon and other convective precipitation over land). In a next step wave properties derived from the GW source model served as input parameters for GW ray tracing. After performing ray tracing simulations from source level, the seasonal shift in momentum flux was also found at higher altitudes. Furthermore, we investigated the dependency of momentum flux distributions, GW drag, and temperature amplitudes on two free tunable parameters—the horizontal scale δ_h and the temporal scale δ_t. For this purpose, three different setups of these parameters were chosen. MF1 and MF2 from *Choi et al.* [2012] account for small- and middle-scale convective cells. Observations from limb-sounding satellites show that there are also larger-scale convective GWs. To also account for these waves that are likely caused by large-scale convection (e.g., in the Asian monsoon), we introduced another setup (MF3) with a spatial scale of 120 km and a time scale of 60 min. A ray tracing simulation which comprises all three source setups showed already good agreement with SABER satellite measurements. Localized features, like the peaks in GW momentum flux above the continents, are consistent with measurements at low latitudes. However, differences were found in the magnitude of momentum flux. This effect was expected, and further improvement could be achieved by introducing an observational filter to account for the limitations of limb-sounding satellites in observing waves of short horizontal wavelength. In particular, limb sounders are not very sensitive to MF1 and MF2. We chose a simple 100 km horizontal cutoff wavelength to limit computational costs. Waves shorter than this wavelength are accounted as invisible to limb-sounding instruments like SABER. As a result, consistency between simulated and observed momentum flux could be further improved. Agreement was found within the observational error margin of the SABER GW retrieval. The last extension and improvement of our model included a

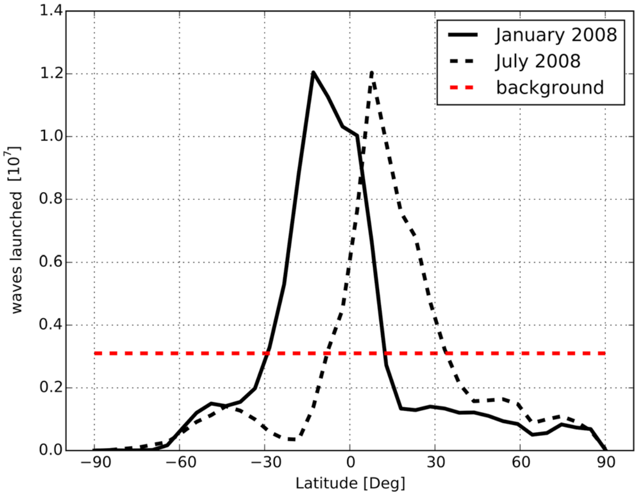

Figure A1. Number of GWs launched from convective sources (black lines) for January 2008 (solid) and July 2008 (dashed). The homogeneous background launch distribution is shown as red dashed line.

background parametrization for middle to high latitudes. The superposition with a background GW spectrum [*Preusse et al.*, 2009] and its resulting momentum flux distributions are in remarkable agreement with observations for the whole latitude range. The simulated global distributions of GW momentum flux, constrained by observations, reproduce all major features found in the relative distribution. Also, momentum fluxes from simulation and observation are consistent within the margin of measurement uncertainties. We therefore conclude that the combination of simulated convective GWs from convective sources in the tropics together with high-latitude background GWs can explain most prominent features in the observed momentum flux. Nevertheless, middle- and high-latitude GWs are still parametrized in our model. Further research on specific sources of nonorographic waves at middle and high latitudes is therefore recommended.

Appendix A: Convective GWs With Background Parametrization

In section 7 we showed results of the convective GW simulation combined with a background parametrization representing other nonorographic GW sources and how this combination significantly improved our simulation results when compared to satellite measurements. The three convective GW launch setups (MF1–MF3) contributed a high amount of longitudinal variation to the momentum flux distribution. This is not reflected by the homogeneous nonorographic launch distribution alone. However, this nonorographic background parametrization has proven to satisfactorily simulate middle- to high-latitude momentum flux [*Preusse et al.*, 2009].

The combination of both launch distributions led to the question of relative weighting between background waves and convective waves. In this study we combined both launch distributions using a linear combination (see equation (7)) with an intermittency between both parametrizations of $\epsilon = 0.1$. Figure A1 shows the result of this linear combination in number of waves launched with the GROGRAT ray tracer as function of latitude. Black lines show convective GWs for January 2008 (solid) and July 2008 (dashed) conditions. The homogeneous background launch distribution is depicted as dashed red line. The figure shows that convective GWs outnumber the background waves by a factor of 4 between 30°S and 30°N. In contrast, background waves dominate the simulation at latitudes beyond 30°N/S. As a result, the overall momentum flux distribution is altered predominantly within the tropics with a decreasing impact toward midlatitudes. Consequently, higher latitudes still show the original momentum flux distribution as, for instance, in *Preusse et al.* [2009].

Acknowledgments
MERRA data were provided by NASA and are available at http://disc.sci.gsfc.nasa.gov/mdisc/. SABER data are available through the web service of GATS Inc. available at http://saber.gats-inc.com/data.php. The work by S. Kalisch is funded by Deutsche Forschungsgemeinschaft (DFG) grant KA4222/2-1. The work by M. Ern was partly supported by Deutsche Forschungsgemeinschaft (DFG) grant PR 919/4-1 (MS-GWaves/SV). We also thank E. Yiğit and two reviewers for their valuable contribution to this paper. H.-Y. Chun was supported by the Korea Meteorological Administration (KMA) Research and Development Program under grant KMIPA 2015-6160.

References

Adler, R. F., et al. (2003), The version 2 Global Precipitation Climatology Project (GPCP) monthly precipitation analysis (1979–present), *J. Hydrometeorol.*, *4*, 1147–1167.

Alexander, M. J., et al. (2010), Recent developments in gravity wave effects in climate models, and the global distribution of gravity wave momentum flux from observations and models, *Q. J. R. Meteorol. Soc.*, *136*, 1103–1124, doi:10.1002/qj.637.

Beres, J. H., M. J. Alexander, and J. R. Holton (2002), Effects of tropospheric wind shear on the spectrum of convectively generated gravity waves, *J. Atmos. Sci.*, *59*, 1905–1824.

Beres, J. H., M. J. Alexander, and J. R. Holton (2004), A method of specifying the gravity wave spectrum above convection based on latent heating properties and background wind, *J. Atmos. Sci.*, *61*(3), 324–337.

Beres, J. H., R. R. Garcia, B. A. Boville, and F. Sassi (2005), Implementation of a gravity wave source spectrum parameterization dependent on the properties of convection in the Whole Atmosphere Community Climate Model (WACCM), *J. Geophys. Res.*, *110*, D10108, doi:10.1029/2004JD005504.

Bosilovich, M. G., F. R. Robertson, and J. Chen (2011), Global energy and water budgets in MERRA, *J. Clim.*, *24*(22), 5721–5739.

Charron, M., E. Manzini, and C. D. Warner (2002), Intercomparison of gravity wave parameterizations: Hines Doppler-spread and Warner and McIntyre ultra-simple schemes, *J. Meteorol. Soc. Jpn.*, *80*, 335–345.

Choi, H.-J., and H.-Y. Chun (2011), Momentum flux spectrum of convective gravity waves. Part I: An update of a parameterization using mesoscale simulations, *J. Atmos. Sci.*, *68*(4), 739–759.

Choi, H. J., H. Y. Chun, and I. S. Song (2009), Gravity wave temperature variance calculated using the ray-based spectral parameterization of convective gravity waves and its comparison with Microwave Limb Sounder observations, *J. Geophys. Res.*, *114*, 2156–2202, doi:10.1029/2008JD011330.

Choi, H.-J., H.-Y. Chun, J. Gong, and D. L. Wu (2012), Comparison of gravity wave temperature variances from ray-based spectral parameterization of convective gravity wave drag with AIRS observations, *J. Geophys. Res.*, *117*, D05115, doi:10.1029/2011JD016900.

Chun, H. Y., and J. J. Baik (1998), Momentum flux by thermally induced internal gravity waves and its approximation for large-scale models, *J. Atmos. Sci.*, *55*, 3299–3310.

Chun, H.-Y., M.-D. Song, J.-W. Kim, and J.-J. Baik (2001), Effects of gravity wave drag induced by cumulus convection on the atmospheric general circulation, *J. Atmos. Sci.*, *58*(3), 302–319.

Chun, H. Y., I. S. Song, J. J. Baik, and Y. J. Kim (2004), Impact of a convectively forced gravity wave drag parameterization in NCAR CCM3, *J. Clim.*, *17*, 3530–3547.

Ern, M., and P. Preusse (2012), Gravity wave momentum flux spectra observed from satellite in the summertime subtropics: Implications for global modeling, *Geophys. Res. Lett.*, *39*, L15810, doi:10.1029/2012GL052659.

Ern, M., P. Preusse, M. J. Alexander, and C. D. Warner (2004), Absolute values of gravity wave momentum flux derived from satellite data, *J. Geophys. Res.*, *109*, D20103, doi:10.1029/2004JD004752.

Ern, M., P. Preusse, J. C. Gille, C. L. Hepplewhite, M. G. Mlynczak, J. M. Russell III, and M. Riese (2011), Implications for atmospheric dynamics derived from global observations of gravity wave momentum flux in stratosphere and mesosphere, *J. Geophys. Res.*, *116*, D19107, doi:10.1029/2011JD015821.

Ern, M., P. Preusse, S. Kalisch, M. Kaufmann, and M. Riese (2013), Role of gravity waves in the forcing of quasi two-day waves in the mesosphere: An observational study, *J. Geophys. Res. Atmos.*, *118*, 3467–3485, doi:10.1029/2012JD018208.

Ern, M., F. Ploeger, P. Preusse, J. C. Gille, L. J. Gray, S. Kalisch, M. G. Mlynczak, J. M. Russell III, and M. Riese (2014), Interaction of gravity waves with the QBO: A satellite perspective, *J. Geophys. Res. Atmos.*, *119*, 2329–2355, doi:10.1002/2013JD020731.

Ern, M., P. Preusse, and M. Riese (2015), Driving of the SAO by gravity waves as observed from satellite, *Ann. Geophys*, *33*(4), 483–504.

Fovell, R., D. Durran, and J. R. Holton (1992), Numerical simulations of convectively generated stratospheric gravity waves, *J. Atmos. Sci.*, *49*, 1427–1442.

Fritts, D. C., and M. J. Alexander (2003), Gravity wave dynamics and effects in the middle atmosphere, *Rev. Geophys.*, *41*, 1003, doi:10.1029/2001RG000106.

Jewtoukoff, V., R. Plougonven, and A. Hertzog (2013), Gravity waves generated by deep tropical convection: Estimates from balloon observations and mesoscale simulations, *J. Geophys. Res. Atmos.*, *118*, 9690–9707, doi:10.1002/jgrd.50781.

Jia, J., P. Preusse, M. Ern, H. Chun, J. Gille, S. Eckermann, and M. Riese (2014), Sea surface temperature as a proxy for convective gravity wave excitation: A study based on global gravity wave observations in the middle atmosphere, *Ann. Geophys.*, *32*, 1373–1394.

Jiang, J. H., B. Wang, K. Goya, K. Hocke, S. D. Eckermann, J. Ma, D. L. Wu, and W. J. Read (2004), Geographical distribution and interseasonal variability of tropical deep convection: UARS MLS observations and analyses, *J. Geophys. Res.*, *109*, D03111, doi:10.1029/2003JD003756.

Kalisch, S., P. Preusse, M. Ern, S. D. Eckermann, and M. Riese (2014), Differences in gravity wave drag between realistic oblique and assumed vertical propagation, *J. Geophys. Res. Atmos.*, *119*, 10,081–10099, doi:10.1002/2014JD021779.

Khouider, B., and M. W. Moncrieff (2015), Organized convection parameterization for the ITCZ*, *J. Atmos. Sci.*, *72*(8), 3073–3096.

Kilpatrick, T. J., and S.-P. Xie (2015), Ascat observations of downdrafts from mesoscale convective systems, *Geophys. Res. Lett.*, *42*, 1951–1958, doi:10.1002/2015GL063025.

Kim, S. Y., H. Y. Chun, and J. J. Baik (2005), A numerical study of gravity waves induced by convection associated with Typhoon Rusa, *Geophys. Res. Lett*, *32*, L24816, doi:10.1029/2005GL024662.

Kim, S. Y., H. Y. Chun, and D. L. Wu (2009), A study on stratospheric gravity waves generated by Typhoon Ewiniar: Numerical simulations and satellite observations, *J. Geophys. Res.*, *114*, D22104, doi:10.1029/2009JD011971.

Kim, Y.-H., A. Bushell, D. Jackson, and H.-Y. Chun (2013), Impacts of introducing a convective gravity-wave parameterization upon the QBO in the Met Office Unified Model, *Geophys. Res. Lett.*, *40*, 1873–1877, doi:10.1002/grl.50353.

Lehmann, C., Y.-H. Kim, P. Preusse, H.-Y. Chun, M. Ern, and S.-Y. Kim (2012), Consistency between Fourier transform and small-volume few-wave decomposition for spectral and spatial variability of gravity waves above a typhoon, *Atmos. Meas. Tech.*, *5*(7), 1637–1651, doi:10.5194/amt-5-1637-2012, [Available at http://www.atmos-meas-tech.net/5/1637/2012/.]

Lindzen, R. S. (1981), Turbulence and stress due to gravity wave and tidal breakdown, *J. Geophys. Res.*, *86*, 9707–9714.

Lindzen, R. S., and J. R. Holton (1968), A theory of the Quasi-Biennial Oscillation, *J. Atmos. Sci.*, *25*, 1095–1107.

Liu, C., S. Shige, Y. N. Takayabu, and E. Zipser (2015), Latent heating contribution from precipitation systems with different sizes, depths, and intensities in the tropics, *J. Clim.*, *28*(1), 186–203.

Liu, H.-L., J. McInerney, S. Santos, P. Lauritzen, M. Taylor, and N. Pedatella (2014), Gravity waves simulated by high-resolution Whole Atmosphere Community Climate Model, *Geophys. Res. Lett.*, *41*, 9106–9112.

Lund, T. S., and D. C. Fritts (2012), Numerical simulations of gravity wave breaking in the lower thermosphere, *J. Geophys. Res.*, *117*, D21105, doi:10.1029/2012JD017536.

Marks, C. J., and S. D. Eckermann (1995), A three-dimensional nonhydrostatic ray-tracing model for gravity waves: Formulation and preliminary results for the middle atmosphere, *J. Atmos. Sci.*, *52*, 1959–1984.

McLandress, C. (1998), On the importance of gravity waves in the middle atmosphere and their parameterization in general circulation models, *J. Atmos. Terr. Phys.*, *60*, 1357–1383.

McLandress, C., M. J. Alexander, and D. L. Wu (2000), Microwave Limb Sounder observations of gravity waves in the stratosphere: A climatology and interpretation, *J. Geophys. Res.*, *105*, 11,947–11,967.

Medvedev, A. S., and G. P. Klaassen (2000), Parameterization of gravity wave momentum deposition based on nonlinear wave interactions: Basic formulation and sensitivity tests, *J. Atmos. Sol. Terr. Phys.*, *62*, 1015–1033.

Mlynczak, M. G. (1997), Energetics of the mesosphere and lower thermosphere and the SABER experiment, *Adv. Space Res.*, *20*, 1177–1183.

Pfister, L., S. Scott, M. Loewenstein, S. Brown, and M. Legg (1993), Mesoscale disturbances in the tropical stratosphere excited by convection: Observations and effects on the stratospheric momentum budget, *J. Atmos. Sci.*, *50*, 1058–1075.

Piani, C., D. Durran, M. J. Alexander, and J. R. Holton (2000), A numerical study of three-dimensional gravity waves triggered by deep tropical convection and their role in the dynamics of the QBO, *J. Atmos. Sci.*, *57*(22), 3689–3702.

Preusse, P. (2001), Satellitenmessungen von Schwerewellen in der mittleren Atmosphäre mit CRISTA, PhD thesis, Univ. of Wuppertal, Germany.

Preusse, P., and M. Ern (2005), Indication of convectively generated gravity waves observed by CLAES, *Adv. Space Res.*, *35*(11), 1987–1991.

Preusse, P., G. Eidmann, S. D. Eckermann, B. Schaeler, R. Spang, and D. Offermann (2001), Indications of convectively generated gravity waves in CRISTA temperatures, *Adv. Space Res.*, *27*(10), 1653–1658.

Preusse, P., A. Dörnbrack, S. D. Eckermann, M. Riese, B. Schaeler, J. T. Bacmeister, D. Broutman, and K. U. Grossmann (2002), Space-based measurements of stratospheric mountain waves by CRISTA: 1. Sensitivity, analysis method, and a case study, *J. Geophys. Res.*, *107*, 8178, doi:10.1029/2001JD000699.

Preusse, P., et al. (2006), Tropopause to mesopause gravity waves in August: Measurement and modeling, *J. Atmos. Sol. Terr. Phys.*, *68*, 1730–1751.

Preusse, P., S. D. Eckermann, M. Ern, J. Oberheide, R. H. Picard, R. G. Roble, M. Riese, J. M. Russell III, and M. G. Mlynczak (2009), Global ray tracing simulations of the SABER gravity wave climatology, *J. Geophys. Res.*, *114*, D08126, doi:10.1029/2008JD011214.

Remsberg, E. E., et al. (2008), Assessment of the quality of the version 1.07 temperature-versus-pressure profiles of the middle atmosphere from TIMED/SABER, *J. Geophys. Res.*, *113*, D17101, doi:10.1029/2008JD010013.

Richter, J. H., F. Sassi, and R. R. Garcia (2010), Toward a physically based gravity wave source parameterization in a general circulation model, *J. Atmos. Sci.*, *67*, 136–156.

Rienecker, M. M., et al. (2011), MERRA: NASA's Modern-Era Retrospective Analysis for Research and Applications, *J. Clim.*, *24*(14), 3624–3648.

Russell, J. M., M. G. Mlynczak, L. L. Gordley, J. Tansock, and R. Esplin (1999), An overview of the SABER experiment and preliminary calibration results, *Proc. SPIE*, *3756*, 277–288, doi:10.1117/12.366382.

Sato, K. (1993), Small-scale wind disturbances observed by the MU radar during the passage of Typhoon Kelly, *J. Atmos. Sci.*, *50*(4), 518–537.

Sato, K., T. Kinoshita, and K. Okamoto (2013), A new method to estimate three-dimensional residual-mean circulation in the middle atmosphere and its application to gravity wave–resolving general circulation model data, *J. Atmos. Sci.*, *70*(12), 3756–3779, doi:10.1175/JAS-D-12-0352.1.

Senf, F., and U. Achatz (2011), On the impact of middle-atmosphere thermal tides on the propagation and dissipation of gravity waves, *J. Geophys. Res.*, *116*, D24110, doi:10.1029/2011JD015794.

Song, I. S., and H. Y. Chun (2005), Momentum flux spectrum of convectively forced internal gravity waves and its application to gravity wave drag parameterization. Part I: Theory, *J. Atmos. Sci.*, *62*, 107–124.

Song, I. S., and H. Y. Chun (2008), A Lagrangian spectral parameterization of gravity wave drag induced by cumulus convection, *J. Atmos. Sci.*, *65*, 1204–1224.

Song, I. S., H. Y. Chun, R. R. Garcia, and B. A. Boville (2007), Momentum flux spectrum of convectively forced internal gravity waves and its application to gravity wave drag parameterization. Part II: Impacts in a GCM (WACCM), *J. Atmos. Sci.*, *64*, 2286–2308.

Suarez, M. J., et al. (2008), The GEOS-5 data assimilation system, *NASA Tech. Rep.*, Goddard Space Flight Center Greenbelt, Md.

Trinh, Q. T., S. Kalisch, P. Preusse, H.-Y. Chun, S. D. Eckermann, M. Ern, and M. Riese (2015a), A comprehensive observational filter for satellite infrared limb sounding of gravity waves, *Atmos. Meas. Tech.*, *8*(3), 1491–1571.

Trinh, Q. T., S. Kalisch, P. Preusse, M. Ern, H.-Y. Chun, S. D. Eckermann, M.-J. Kang, and M. Riese (2016), Tuning of a convective gravity wave source scheme based on HIRDLS observations, *Atmos. Chem. Phys.*, *16*(11), 7335–7356, doi:10.5194/acp-16-7335-2016.

Yee, J. H., E. R. Talaat, A. B. Christensen, T. L. Killeen, J. M. Russell, and T. N. Woods (2003), TIMED instruments, *Johns Hopkins APL Tech. Dig.*, *24*, 156–164.

Yiğit, E., A. D. Aylward, and A. S. Medvedev (2008), Parameterization of the effects of vertically propagating gravity waves for thermosphere general circulation models: Sensitivity study, *J. Geophys. Res.*, *113*, D19106, doi:10.1029/2008JD010135.